Chapter 2
A Unified Plasticity Model for Large Post-liquefaction Shear Deformation of Sand and Its Numerical Implementation

This chapter builds on the work of Zhang and Wang (2012) to present the formulation of a unique model that (1) achieves the simulation of post-liquefaction shear deformation based on its physics, allowing the unified description of pre- and post-liquefaction behaviour of sand; (2) directly links the cyclic mobility of sand with reversible and irreversible dilatancy, enabling the unified description of monotonic and cyclic loading; (3) introduces critical state soil mechanics concepts to achieve unified modelling of sand under different states. Modelling of large post-liquefaction shear deformation is achieved based on the physics proposed by Zhang and Wang. The proposed model is able to appropriately describe some important features of sand, including dilatancy during loading and unloading, and softening of dense sand. The model is first described in triaxial stress space, and then generalized into multiaxial stress space with three dimensional mapping rules for the calculation of plasticity and dilatancy. The determination of the model parameters is described. The cutting-plane stress integration scheme and the Pegasus procedure for the three dimensional implementation of the model into the finite-element framework OpenSees (McKenna and Fenves 2001) are presented in detail. The OpenSees platform is chosen for its great capabilities in geotechnical earthquake engineering simulation and most importantly for the model to be openly available to the technical community. Finally, the performance of the model and its three dimensional implementation is evaluated by simulations of classical drained and undrained triaxial experiments on Toyoura sand by Verdugo and Ishihara (1996) and undrained cyclic torsional experiments on Toyoura sand. Simulations of the VELACS centrifuge shaking table tests are also carried out.

R. Wang, *Single Piles in Liquefiable Ground*, Springer Theses,
DOI 10.1007/978-3-662-49663-3_2

2.1 Model Formulation in Triaxial Stress Space

A description of the proposed constitutive model is first provided in triaxial stress space. The model operates within the framework of bounding surface plasticity proposed by Dafalias and Popov (1975) and adopts features of the hypoplasticity model developed by Wang et al. (1990). The model uses the two dilatancy induced volumetric strain components for the successful description of the dilatancy behaviours of sand in both monotonic and cyclic loading, and accounts for the generation of post-liquefaction shear deformation at zero effective confining stress based on the physics of post-liquefaction deformation proposed by Zhang and Wang (2012). Critical state soil mechanics principles were incorporated into the model to allow unified description of sand by introducing the state parameter (Been and Jefferies 1985).

In the current model framework, mean effective pressure change induced volumetric strain is assumed to be elastic and shear induced volumetric strain is assumed to be fully plastic, matching the decomposition of volumetric strain stated previously in Eq. (1.1) with traditional elastic and plastic decompositions.

2.1.1 Basic Equations

The incremental stress-strain relations follow the typical equations for elastic-plasticity:

$$\dot{\varepsilon}_q^e = \frac{\dot{q}}{3G}; \quad \dot{\varepsilon}_v^e = \frac{\dot{p}}{K} \tag{2.1}$$

$$\dot{\varepsilon}_q^p = \frac{\dot{\eta}}{H}; \quad \dot{\varepsilon}_v^p = D\left|\dot{\varepsilon}_q^p\right| \tag{2.2}$$

where the elastic and plastic strains are denoted by superscripts e and p respectively. G and K are the elastic shear and bulk moduli, H is the plastic shear modulus and D dilatancy rate.

The model neglects the plastic volumetric strains during constant stress ratio loading for simplicity, though this proposition would cause underestimation of the reconsolidation settlement of soil. The elastic volumetric strain ε_v^e corresponds to the mean effective stress change induced volumetric strain ε_{vc}, and ε_v^p corresponds to the dilatancy induced volumetric strain $\varepsilon_{vd,ir} + \varepsilon_{vd,re}$ in Eq. (1.1).

2.1.2 Elastic Moduli

The elastic shear and bulk moduli are defined as suggested by Richart et al. (1970):

$$G = G_o \frac{(2.973 - e_{in})^2}{1 + e_{in}} p_a \left(\frac{p}{p_a}\right)^{\frac{1}{2}} \tag{2.3}$$

$$K = \frac{1 + e_{in}}{\kappa} p_a \left(\frac{p}{p_a}\right)^{\frac{1}{2}} \tag{2.4}$$

where e_{in} is the initial void ratio, p_a is the atmospheric pressure for normalization, G_o and κ are material constants. The elastic moduli were defined using the initial void ratio so that elastic volumetric strain is strictly dependent only on effective stress, which decouples the elastic moduli with shear induced volumetric strains. Thus making it consistent with our decomposition of volumetric strains.

2.1.3 State Parameter

For the incorporation of critical state behaviour, and for the unified description of sand at various densities with a same set of parameters, the state parameter Ψ proposed by Been and Jefferies (1985) is introduced to consider the dependency of sand behaviour on the current state.

$$\Psi = e - e_c \tag{2.5}$$

with e being the current void ratio and e_c the critical void ratio. At critical state, Roscoe et al. (1958) and Schofield and Wroth (1968) proposed that $e = e_c$ and $q_c/p_c = M$, where M is defined as the critical stress ratio as shown in Fig. 2.1. The relationship between the critical void ratio e_c and mean effective stress is determined using Li and Wang's (1998) power formulation which have proved effective for various types of sands (Li and Wang 1998; Ling and Yang 2006):

$$e_c = e_0 - \lambda_c (p_c/p_{at})^{\xi} \tag{2.6}$$

where e_0 is the void ratio at $p_c = 0$ and λ_c and ξ are constants. By correct consideration for the variation of plasticity and dilatancy with the state parameter, the model is applicable to different pressures and densities using a single set of parameters.

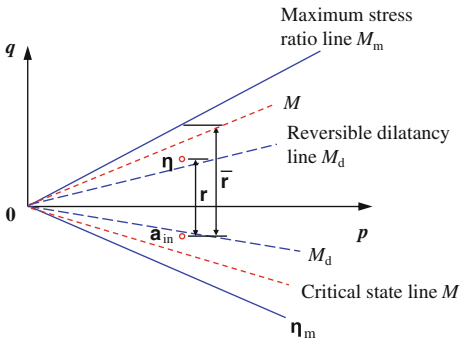

Fig. 2.1 Schematic illustration of critical state, maximum stress ratio and reversible dilatancy lines with mapping rules in triaxial stress space

2.1.4 Plastic Loading and Load Reversal

By adopting Wang's (1990) hypoplasticity approach, plastic loading and load reversal is determined by the sign of:

$$l = \dot{\eta}(\eta - \alpha_{in}) \tag{2.7}$$

where α_{in} is the stress ratio at the previous load reversal. Plastic loading is induced when $l > 0$, and load reversal occurs at $l < 0$.

2.1.5 Plastic Modulus

The plastic modulus and relevant mapping rules in the model are modified from the work of Wang et al. (1990). The peak mobilized stress ratio, which has been shown to be dependent on the state parameter (Been and Jefferies 1985), is here defined using an exponential variation with Ψ as proposed by Li and Dafalias (2000) to be $M_p = M\exp(-n^b\Psi)$. A maximum stress ratio (M_m) surface is proposed to define the mapping rule, as shown in Fig. 2.1 in triaxial stress space. By using the peak mobilized and maximum stress ratios, the plastic modulus can be determined in a way that is related to the bounding surface plasticity concept. Thus, the plastic modulus is expressed as:

$$H = \frac{h}{p}G\exp(-n^p\Psi)\left(\frac{M\exp(-n^p\Psi)}{M_m}\left(\frac{\bar{\rho}}{\rho}\right) - 1\right) \tag{2.8}$$

where h is a model parameter; n^p is a model constant; ρ is the distance from the current stress ratio η to α_{in}; and $\bar{\rho}$ is the distance between the projection of current stress on the maximum stress ratio surface and α_{in} (Fig. 2.1).

The maximum stress ratio M_m surface is defined to expand according to the maximum stress ratio that has occurred during loading, until it reaches the peak

mobilized stress ratio $M\exp(-n^b\Psi)$. Once the current stress ratio reaches outside $M\exp(-n^b\Psi)$, the maximum stress ratio follows the current stress ratio until it falls on the peak mobilized stress ratio again. Through this formulation, the plastic modulus $H = 0$ is satisfied at the critical state and the softening response where $H < 0$ is also made possible when the stress ratio exceeds the peak mobilized stress ratio M_p.

2.1.6 Dilatancy

The determination of dilatancy is a unique part of the proposed model. According to the propositions made by Shamoto and Zhang (1997) and Zhang (1997), the dilatancy of sand is decomposed into a reversible and an irreversible component, through which the dilatancy during load reversal and cyclic loading can be properly reflected. In this model, the dilatancy rate D is determined by combining the reversible part D_{re} and irreversible part D_{ir}:

$$D = \frac{\dot{\varepsilon}_v^p}{|\dot{\varepsilon}_q^p|} = D_{re} + D_{ir} = \frac{\dot{\varepsilon}_{vd,re}}{|\dot{\varepsilon}_q^p|} + \frac{\dot{\varepsilon}_{vd,ir}}{|\dot{\varepsilon}_q^p|} \tag{2.9}$$

Through experimental observations Zhang and Wang (2012) pointed out that reversible dilatancy remained on the expansion side, generating and releasing during loading and unloading cycles. The generation and release rate of reversible dilatancy are here defined using separate equations. The generation rate of reversible dilatancy, for which $D_{re,gen}$ is negative, is defined in a form similar to Rowe's (1962) dilatancy theory:

$$D_{re,gen} = d_{re,1}(M_d - \eta) \tag{2.10}$$

where $d_{re,1}$ is a reversible dilatancy parameter, and $M_d = M\exp(n^d\Psi)$ is the stress ratio at which reversible dilatancy changes from contraction to expansion, and also follows an exponential variation with Ψ (Li and Dafalias 2000), shown as the reversible dilatancy line in Fig. 2.1. Reversible dilatancy remains non-positive and is released after load reversal, the release rate is defined as:

$$D_{re,rel} = \left(d_{re,2}\chi\right)^2/p \tag{2.11}$$

$d_{re,2}$ is another dilatancy parameter used to calculate the release of reversible dilatancy. $\chi = \min(-d_{ir}\frac{\varepsilon_{vd,re}}{\varepsilon_{vd,ir}^{pr}}, 1)$ is a function controlling the reversible dilatancy release process, where d_{ir} is an irreversible dilatancy constant and $\varepsilon_{vd,ir}^{pr}$ is the $\varepsilon_{vd,ir}$ at previous load reversal. This function χ guarantees $D_{re,rel}$ to be zero when $\varepsilon_{vd,re}$ is completely released, and restricts the release rate from becoming overly large, thus avoiding the overestimation of contraction upon load reversal. Note that prior to the

first load reversal, χ is set as 0 and the release rate $D_{re,rel}$ is constantly 0. Reversible dilatancy can thus be expressed together as:

$$D_{re} = \frac{\dot{\varepsilon}_{vd,re}}{|\dot{\varepsilon}_q^p|} = \begin{cases} D_{re,gen}, & |\eta| \geq M_{d,c/e} \quad \& \quad |\dot{\eta}| > 0 \\ D_{re,rel}, & |\eta| < M_{d,c/e} \quad \text{or} \quad |\dot{\eta}| < 0 \end{cases} \tag{2.12}$$

It has been observed that the irreversible dilatancy induced volumetric strain $\varepsilon_{vd,ir}$ remains contractive, and followed the pattern of accumulating asymptotically during loading with a decreasing rate during each monotonic shearing since the last stress reversal. Irreversible dilatancy rate D_{ir} is defined to satisfy these features as:

$$\begin{aligned} D_{ir} &= \frac{\dot{\varepsilon}_{vd,ir}}{|\dot{\varepsilon}_q^p|} \\ &= d_{ir} \exp(n^d \Psi - \alpha \varepsilon_{vd,ir}) \left(< M_d - \eta > \exp(\chi) + \left(\frac{\gamma_{d,r} < 1 - \exp(n^d \Psi) >}{\gamma_{d,r} < 1 - \exp(n^d \Psi) > + \gamma_{mono}} \right)^2 \right) \end{aligned} \tag{2.13}$$

Here α is a parameter controlling the decrease rate of irreversible dilatancy, γ_{mono} is the shear strain since the last stress reversal and $\gamma_{d,r}$ is a reference shear strain. $\langle\rangle$ are the MacCauley brackets that yield $\langle x \rangle = x$ if $x > 0$ and $\langle x \rangle = 0$ if $x \leq 0$. The $\exp(n^d \Psi - \alpha \varepsilon_{vd,ir})$ part of the equation reflects asymptotic accumulation of irreversible dilatancy, and the part $\left(\frac{\gamma_{d,r} < 1 - \exp(n^d \Psi) >}{\gamma_{d,r} < 1 - \exp(n^d \Psi) > + \gamma_{mono}} \right)^2$ reflects the decreasing dilatancy rate during each monotonic loading process. By introducing $< M_d - \eta >$ into the formulation, the initial contraction during loading can be appropriately reflected, and $\exp(\chi)$ enhances the contraction upon load reversal. The incorporation of state parameter allows the formulation to take density and effective pressure into consideration and comply with critical state soil mechanic principles.

A most significant result of incorporating the state parameter in the definition of plastic modulus, reversible and irreversible dilatancy is that the model becomes fully compatible with critical state soil mechanics requirements and capable of simulating the behaviour of sand at various densities with the same set of material constants. The unique formulation of plastic modulus and dilatancy rates allows for the appropriate simulation of both monotonic and cyclic loading. These features will be shown in the simulations later in this chapter.

2.1.7 Post-liquefaction Shear Deformation

As plasticity caused by constant η loading is neglected in this model, the volumetric strain caused by mean effective stress change ε_{vc} proposed by Zhang and Wang (2012) in Eq. (2.1) matches ε_v^e in Eq. (2.1). By substituting Eq. (2.4) into Eq. (2.1)

and integrating from the current effective stress p to zero effective stress, the threshold ε_{vc} at which zero effective stress is reached is expressed as a function of p:

$$\varepsilon_{vc,0} = f(p) = -\frac{2\kappa}{1+e_{in}}\left(\frac{p}{p_a}\right)^{\frac{1}{2}} \tag{2.14}$$

Based on Zhang and Wang's (2012) theory, once the current ε_{vc} (or ε_v^e) decreases beyond the threshold value $\varepsilon_{vc,0}$, sand liquefies and p remains constant at 0, $\dot{\varepsilon}_v^e = \frac{\dot{p}}{K}$ in Eq. (2.1) becomes invalid and ε_{vc} is then determined by the volumetric compatibility equation Eq. (1.1) and is able to exceed $\varepsilon_{vc,0}$.

For sand to exit the state of liquefaction when $\varepsilon_{vc} < \varepsilon_{vc,0}$, sufficient dilation must occur for ε_{vc} to become greater than $\varepsilon_{vc,0}$ again. According to the dilation equation in Eq. (2.2), sufficient dilation would depend on the shear strain ε_q^p generated at liquefaction state, which is the cause of large post-liquefaction shear deformation:

$$\varepsilon_v^p = \int (D_{ir} + D_{re}) d\left|\varepsilon_q^p\right| \tag{2.15}$$

2.2 Multiaxial Generalization

With the model presented fully in triaxial stress space, its multiaxial generalization is then possible. The basic equations for the multiaxial generalization are:

$$\dot{\varepsilon}_v^e = \frac{\dot{p}}{K}; \quad \dot{\mathbf{e}}^e = \frac{\dot{\mathbf{s}}}{2G} \tag{2.16}$$

$$\dot{\varepsilon}_v^p = \langle L \rangle D; \quad \dot{\mathbf{e}}^p = \langle L \rangle \mathbf{m} \tag{2.17}$$

$p = \mathrm{tr}(\boldsymbol{\sigma})/3$ is the mean effective stress, with $\boldsymbol{\sigma}$ being the effective stress tensor; $\mathbf{s} = \boldsymbol{\sigma} - p\mathbf{I}$ is the deviatoric stress, $\mathbf{I}$ being the rank two identity tensor; $\varepsilon_v = \mathrm{tr}(\boldsymbol{\varepsilon})$ is the volumetric strain, $\boldsymbol{\varepsilon}$ being the strain tensor; $\mathbf{e} = \boldsymbol{\varepsilon} - \varepsilon_v/3\mathbf{I}$ is the deviatoric strain tensor. L is the plastic loading index and $\mathbf{m}$ the deviatoric strain flow direction. The deviatoric stress ratio tensor is here defined as $\mathbf{r} = \frac{\mathbf{s}}{p}$, and $q = \sqrt{\frac{3}{2}\mathbf{s} : \mathbf{s}}$, $\eta = \frac{q}{p}$.

The total stress-strain relation can be formulated by combining Eqs. (2.16) and (2.17) to be:

$$\dot{\varepsilon} = \frac{1}{2G} p\dot{\mathbf{r}} + \left(\frac{1}{2G}\mathbf{r} + \frac{1}{3K}\mathbf{I}\right)\dot{p} + \left(\mathbf{m} + \frac{D}{3}\mathbf{I}\right)\langle L \rangle \tag{2.18}$$

with the elastic moduli G and K still defined by Eqs. (2.3) and (2.4).

The critical, maximum stress ratio and reversible dilatancy surfaces shown schematically in Fig. 2.2 are defined by:

$$f_c(\boldsymbol{\sigma}) = \eta - Mg(\theta) = 0 \tag{2.19}$$

$$f_m(\boldsymbol{\sigma}) = \eta - M_m g(\theta) = 0 \tag{2.20}$$

$$f_d(\boldsymbol{\sigma}) = \eta - M_d g(\theta) = 0 \tag{2.21}$$

where θ is the lode angle calculated according to:

$$\theta = \frac{1}{3}\sin^{-1}\left(-\frac{\mathbf{s}:\mathbf{s}:\mathbf{s}}{6q}\right) \tag{2.22}$$

The function $g(\theta)$ in this model follows Zhang's (1997) proposition which showed excellent agreement with test data, and is defined as:

$$g(\theta) = \frac{1}{1 + M_p(1 + \sin 3\theta - \cos^2 3\theta)/6 + (M_p - M_{p,o})\cos^2 3\theta / M_{p,o}} \tag{2.23}$$

$$M_p = \frac{6\sin\phi_f}{3 - \sin\phi_f} \tag{2.24}$$

$$M_{p,o} = \frac{2\sqrt{3}\tan\phi_f}{\sqrt{3 + 4\tan^2\phi_f}} \tag{2.25}$$

$M_p = M\exp(-n^b\Psi)$ is the peak mobilized stress ratio at triaxial compression and ϕ_f is the corresponding friction angle, $M_{p,o}$ is the peak mobilized stress ratio under torsional shear after isotropic consolidation.

Similar to the triaxial space formulation, plastic loading is determined in three dimensional space by the load index L:

$$L = \frac{\mathbf{L}:\underline{\sigma}}{H} = \frac{p\underline{\mathbf{r}}:\mathbf{n}}{H} \tag{2.26}$$

Here $\mathbf{n}$ is a unit deviatoric tensor serving as the loading direction in deviatoric stress space in the model, and the loading direction $\mathbf{L}$ is defined as $\mathbf{L} = \mathbf{n} - \frac{1}{3}(\mathbf{n}:\mathbf{r})\mathbf{I}$. Plastic loading is induced when $L > 0$, and load reversal occurs at $L < 0$.

It is further assumed that the deviatoric strain flow direction $\mathbf{m}$ in Eq. (2.17) is the same as the loading direction in deviatoric stress space so as:

$$\mathbf{m} = \mathbf{n} = \bar{\mathbf{r}}/\sqrt{\bar{\mathbf{r}}:\bar{\mathbf{r}}} \tag{2.27}$$

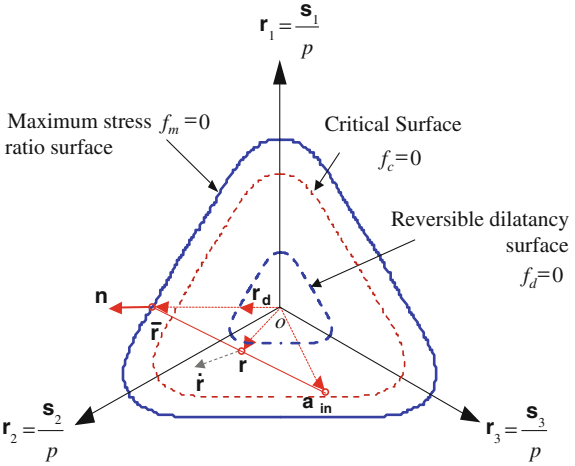

Fig. 2.2 Schematic illustration of critical state, maximum stress ratio and reversible dilatancy surfaces with mapping rules

Here $\bar{\mathbf{r}}$ represents the projection of the current stress point on the maximum stress ratio surface in deviatoric stress space (Fig. 2.2), the mapping rule for this projection is adopted from the work of Wang et al. (1990). As shown in Fig. 2.2, the projection of current stress ratio on the maximum stress ratio surface $\bar{\mathbf{r}}$ is defined as the intersection between the extension of the line from the previous load reversal point $\boldsymbol{\alpha}_{\mathbf{in}}$ to $\mathbf{r}$ and the maximum stress ratio surface:

$$\bar{\mathbf{r}} = \boldsymbol{\alpha}_{\mathbf{in}} + \beta(\mathbf{r} - \boldsymbol{\alpha}_{\mathbf{in}}) \tag{2.28}$$

where β can be solved by substituting Eq. (2.27) into Eq. (2.19). It needs pointing out that although theoretically $\mathbf{n}$ should be the unit normal to the maximum stress ratio surface in deviatoric stress ratio space, due to the numerical difficulty in calculating the normal to the surface, a compromise is made for the model to be numerically applicable by setting the deviatoric loading and flow directions to be the same as $\bar{\mathbf{r}}$ (Fig. 2.2), which is the same approach taken by Andrianopoulos et al. (2010).

When the loading index L is positive, plastic loading occurs. Once L becomes negative, load reversal takes place and the projection centre $\boldsymbol{\alpha}_{\mathbf{in}}$ is updated to be the current stress ratio.

The plastic modulus H can then be defined based on the mapping rule and Eq. (2.8):

$$H = \frac{2}{3} hg(\bar{\theta}) G \exp(-n^p \Psi) \left(\frac{M \exp(-n^b \Psi)}{M_m} \left(\frac{\bar{\rho}}{\rho} \right) - 1 \right) \tag{2.29}$$

where the factor $\frac{2}{3}$ is for the equation to be compatible with that in triaxial stress space, $\bar{\rho}$ is the distance between $\bar{\mathbf{r}}$ and $\boldsymbol{\alpha}_{\mathbf{in}}$, and ρ the distance between $\mathbf{r}$ and $\boldsymbol{\alpha}_{\mathbf{in}}$.

The mapping rule for reversible dilatancy is defined so that the projection of the current stress ratio on the reversible dilatancy surface $\mathbf{r_d}$ is the intersection between $\bar{\mathbf{r}}$ and the reversible dilatancy surface:

$$\mathbf{r_d} = \frac{M_d}{M_m}\bar{\mathbf{r}} = \frac{M\exp(n^d\Psi)}{M_m}\bar{\mathbf{r}} \tag{2.30}$$

The generation and release of reversible dilatancy can then be judged by the angle between $\mathbf{r_d} - \mathbf{r}$ and $\mathbf{n}$:

$$D_{re} = \frac{\dot{\varepsilon}_{vd,re}}{\dot{\gamma}^p} = \begin{cases} D_{re,gen}, & (\mathbf{r_d}-\mathbf{r})\mathbf{:}\,\mathbf{n} < 0 \\ D_{re,rel}, & (\mathbf{r_d}-\mathbf{r})\mathbf{:}\,\mathbf{n} > 0 \end{cases} \tag{2.31}$$

While the release rate still follows the triaxial formulation Eq. (2.11), the generation rate of reversible dilatancy now becomes:

$$D_{re,gen} = \sqrt{\frac{2}{3}}d_{re,1}(\mathbf{r_d}-\mathbf{r})\mathbf{:}\,\mathbf{n} \tag{2.32}$$

$\sqrt{\frac{2}{3}}$ is introduced for consistency with the formulation in triaxial stress space.

Irreversible dilatancy rate D_{ir} defined in the triaxial formulation by Eq. (2.13) is still valid in the multiaxial formulation. The generation of post-liquefaction shear deformation also follows the description in the triaxial stress space formulation.

2.3 Determination of Model Parameters

Table 3.1 lists the 14 parameters used in the model. Some parameters used in this model have been documented by previous researchers, including the elastic modulus constants (G_0, κ) (Zhang and Wang 2012; Richart et al. 1970), plastic modulus parameter (h) (Wang et al. 1990) and critical state parameters (M, λ_c, e_0, ξ) (Li and Dafalias 2000), the calibration methods suggested for these parameters in the respective studies can be adopted.

The state parameter constants n^p and n^d can be determined through $n^p = \ln(M/\eta_p)/\Psi_p$ and $n^d = \ln(M_d/M)/\Psi_d$ derived from Eqs. (2.8) and (2.10), where η_p and Ψ_p are η and Ψ at peak stress ratio in a monotonic drained triaxial test, and M_d and Ψ_d are those at reversible dilatancy sign change points.

It is important to note here that the determination method of n^d is different to that suggested by Li and Dafalias (2000) due to the way dilatancy is defined in this dissertation. Drained cyclic torsional or triaxial tests should be used for the determination of n^d here, as M_d can only be acquired once irreversible dilatancy is negligible after a number of loading cycles. For example, Fig. 2.3 shows the stress ratio and reversible dilatancy component relations after 18 cycles of a drained cyclic

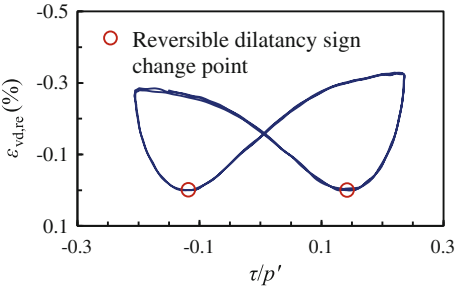

Fig. 2.3 Stress ratio and reversible dilatancy component relations after 18 cycles of a drained cyclic torsional test for Toyoura sand (data from Shamoto and Zhang 1997)

torsional test for Toyoura sand. At this stage, irreversible dilatancy becomes negligible, and M_d can be determined from the figure to be 0.222. Using the critical state parameters for Toyoura sand given by Li and Wang (1998), the state parameter Ψ_d at this state is −0.232, thus yielding a n^d of 7.8 for Toyoura sand.

The reversible dilatancy parameters $d_{re,1}$ can be determined using the relationship between η and $\frac{d\varepsilon_{vd}}{d\gamma^p}$ from drained cyclic tests as suggested by Zhang and Wang (2012), and $d_{re,2}$ should then be chosen to ensure the release of reversible dilatancy.

For the irreversible dilatancy parameters (d_{ir} and α especially, γ_{dr} can generally be set at 0.05), a trial-and-error process should be adopted to simulate the stress strain behaviour of undrained cyclic torsional/triaxial tests of different initial confining pressure or shear stress amplitude, as was described by Zhang and Wang (2012). The parameter d_{ir} mainly determines how fast liquefaction is reached in undrained cyclic tests, and α controls the decrease rate of irreversible dilatancy.

2.4 Model Implementation

The constitutive model is implemented into the open source finite element framework OpenSees (McKenna and Fenves 2001) using a cutting plane algorithm (Simo and Ortiz 1985) with substepping for the stress integration scheme. Solid-fluid coupled elements needed for the undrained and partially drained analysis of sand, which is essential for liquefaction analysis, are already incorporated into OpenSees [e.g. u-p elements by Yang et al. (2008) and SSP u-p elements by McGann et al. (2012)].

2.4.1 Numerical Treatment for Zero Effective Stress State

In the implementation of the model, to avoid numerical difficulties at zero effective stress during liquefaction, a $p_{\min}$ is set as the minimum effective confining pressure, thus for p to be:

$$\begin{cases} \dot{p} = K\dot{\varepsilon}_v^e, & \varepsilon_{vc} > \varepsilon_{vc,0} \\ p = p_{\min}, & \varepsilon_{vc} \le \varepsilon_{vc,0} \end{cases} \tag{2.33}$$

The threshold mean effective stress change induced volumetric strain then becomes:

$$\varepsilon_{vc,0} = -\frac{2\kappa}{1+e}\left(\left(\frac{p}{p_a}\right)^{\frac{1}{2}} - \left(\frac{p_{\min}}{p_a}\right)^{\frac{1}{2}}\right) \tag{2.34}$$

The effectiveness of this approach has been validated by Zhang and Wang (2012).

2.4.2 Stress Integration Scheme

The cutting-plane algorithm was chosen for its simplicity and efficiency, being a semi-explicit integration scheme, relatively small time increments are needed for stability. To increase stability, a substepping technique is proposed.

At the beginning of each step, the strain increment from the global converged state is used to calculate an elastic prediction of stress increment, note once again $\varepsilon_{vc} = \varepsilon_v^e$ and p is expressed as a function of ε_{vc}:

$$(\varepsilon_{vc})_{n+1}^{trial} = (\varepsilon_{vc})_n + (\Delta\varepsilon_v)_{n+1} \tag{2.35}$$

$$p_{n+1}^{trial} = g((\varepsilon_{vc})_{n+1}^{trial}) = \begin{cases} p_a((\frac{p_{in}}{p_a})^{\frac{1}{2}} + \frac{1+e_{in}}{2k}(\varepsilon_{vc})_{n+1}^{trial})^2, & (\varepsilon_{vc})_{n+1}^{trial} > \varepsilon_{vc,0} \\ p_{\min}, & (\varepsilon_{vc})_{n+1}^{trial} \le \varepsilon_{vc,0} \end{cases} \tag{2.36}$$

$$\mathbf{s}_{n+1}^{trial} = \mathbf{s}_n + 2G_{n+1}^{trial}\Delta\mathbf{e}_{n+1} \tag{2.37}$$

where n is the current step and $n + 1$ the next step. The elastic prediction of stress increment along with the shear strain increment is used to determine the number of sub-steps needed:

$$n_{sub} = \max(\lceil \Delta\gamma_{n+1}/tolerance1 \rceil, \lceil \Delta\eta_{n+1}/tolerance2 \rceil) \tag{2.38}$$

where $\Delta\gamma_{n+1} = \sqrt{\frac{2}{3}\Delta\mathbf{e}_{n+1} : \Delta\mathbf{e}_{n+1}}$, $tolerance1$ and $tolerance2$ are the tolerable shear strain and shear stress invariable increment in each sub-step, $\lceil\ \rceil$ is a round up function.

After determining the number of sub-steps, the strain increment at each sub-step is acquired through dividing the strain increment by n_{sub}. The cutting-plane algorithm is then used for the stress integration during each sub-step. Figure 2.4 provides a graphical illustration of the cutting-plane algorithm. The main concept of

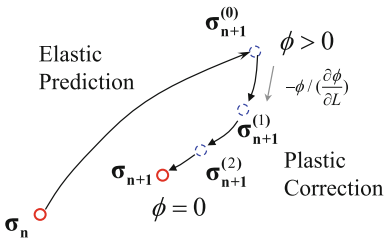

Fig. 2.4 Schematic illustration of the cutting plane stress integration algorithm

the cutting plane algorithm is to first make an elastic estimate of the stress increment and then bring the stress back to the solution through plastic correction by enforcing the consistency condition $\phi = 0$ using the first order Taylor series expansion of the consistency condition during each iteration (Fig. 2.4). The main steps of the algorithm are as follows.

1. Initialize the local iteration number k, plastic strain increment and loading index

$$k = 0; \quad (\dot{\varepsilon}_v^p)_{n+1}^{(k)} = 0; \quad (\dot{\mathbf{e}}^p)_{n+1}^{(k)} = 0; \quad L = 0; \tag{2.39}$$

2. Elastic prediction of stress state at next step

$$(\varepsilon_{vc})_{n+1}^{(k)} = (\varepsilon_{vc})_n + (\Delta\varepsilon_v)_{n+1} \tag{2.40}$$

$$p_{n+1}^{(k)} = g((\varepsilon_{vc})_{n+1}^{(k)}); \quad \mathbf{s}_{n+1}^{(k)} = \mathbf{s}_n + 2G_{n+1}^{(k)}\Delta\mathbf{e}_{n+1} \tag{2.41}$$

3. Check consistency condition to determine whether plastic loading or load reversal occurs

$$\phi^{(k)} = (\mathbf{s}_{n+1}^{(k)} - \mathbf{s}_n)\mathbf{:}\,\mathbf{n}_{n+1}^{(k)} - (p_{n+1}^{(k)} - p_n)\mathbf{r}_n\mathbf{:}\,\mathbf{n}_{n+1}^{(k)} - LH_{n+1}^{(k)} \tag{2.42}$$

If $\phi^{(k)} > 0$, plastic loading is induced, go to step 4; else, load reversal happens and stress-strain relationship at current step is assumed to be elastic, the projection centre is updated, $(\boldsymbol{\alpha}_{\mathbf{in}})_{n+1} = \mathbf{r}_n$, go to step 6.

4. Plastic correction through the calculation of loading index increment, as shown in Fig. 2.4

$$\Delta L^{(k)} = -\phi^{(k)}/(\frac{\partial\phi}{\partial L})^{(k)} = \frac{\phi^{(k)}}{H_{n+1}^{(k)} + 2G_{n+1}^{(k)} - K_{n+1}^{(k)}D_{n+1}^{(k)}(\mathbf{r}_{n+1}^{(k)}\mathbf{:}\,\mathbf{n}_{n+1}^{(k)})} \tag{2.43}$$

Update loading index and stress-strain state

$$L^{(k+1)} = L^{(k)} + \Delta L^{(k)} \tag{2.44}$$

$$(\Delta\varepsilon_v^p)_{n+1}^{(k+1)} = L^{(k+1)} D_{n+1}^{(k)}; \quad (\Delta\mathbf{e^p})_{n+1}^{(k+1)} = L^{(k+1)}\mathbf{n}_{n+1}^{(k)} \tag{2.45}$$

$$(\varepsilon_{vc})_{n+1}^{(k+1)} = (\varepsilon_{vc})_n + ((\Delta\varepsilon_v)_{n+1} - (\Delta\varepsilon_v^p)_{n+1}^{(k+1)}) \tag{2.46}$$

$$p_{n+1}^{(k+1)} = g((\varepsilon_{vc})_{n+1}^{(k+1)}); \quad \mathbf{s}_{n+1}^{(k+1)} = \mathbf{s}_n + 2G_{n+1}^{(k+1)}(\Delta\mathbf{e}_{n+1} - (\Delta\mathbf{e}^p)_{n+1}^{(k+1)}) \tag{2.47}$$

5. Check residual of consistency condition for convergence

$$\phi^{(k+1)} = \Delta\mathbf{s}_{n+1}^{(k+1)} : \mathbf{n}_{n+1}^{(k+1)} - \Delta p_{n+1}^{(k+1)}\mathbf{r}_n : \mathbf{n}_{n+1}^{(k+1)} - L_{n+1}^{(k+1)} H_{n+1}^{(k+1)} \tag{2.48}$$

If $\left|\phi^{(k+1)}\right| > tolerance$, convergence is not reached, $k = k+1$ and go to step 4; else go to step 6.

6. Update stress, strain and internal variables

$$p_{n+1} = p_{n+1}^{(k+1)}; \quad \mathbf{s}_{n+1} = \mathbf{s}_{n+1}^{(k+1)}; \quad (\varepsilon_{vc})_{n+1} = (\varepsilon_{vc})_{n+1}^{(k+1)} \tag{2.49}$$

As the cutting-plane algorithm is semi-explicit, the continuum tangent operator is used in the solution of the global finite element equations:

$$\boldsymbol{\sigma}_{n+1} = \boldsymbol{\sigma}_n + \mathbf{D}_{ep} : \Delta\boldsymbol{\varepsilon}_{n+1} \tag{2.50}$$

$$\mathbf{D}_{ep} = \mathbf{D}_e - \frac{\mathbf{D}_e : (\mathbf{m} + \frac{D_{ir}+D_{rc}}{3}\mathbf{I}) \otimes (\mathbf{n} - \frac{1}{3}(\mathbf{r} : \mathbf{n})\mathbf{I}) : \mathbf{D}_e}{H + (\mathbf{n} - \frac{1}{3}(\mathbf{r} : \mathbf{n})\mathbf{I}) : \mathbf{D}_e : (\mathbf{m} + \frac{D_{ir}+D_{rc}}{3}\mathbf{I})} \tag{2.51}$$

where $\mathbf{D}_e$ is the elastic tangent operator.

2.4.3 Determination of Projection Point on Maximum Stress Ratio Surface

For the three dimensional implementation of the model, the determination of the projection of the current stress state on the maximum stress ratio surface is needed. As analytically solving β in Eq. (2.27) is of some difficulty, in the implementation β is solved numerically using the Pegasus procedure developed Dowel and Jarratt (1972) guaranteeing fast unconditional convergence, which has been used in the implementation of constitutive models by Sloan et al. (2001) and Andrianopoulos et al. (2010). The main steps of the procedure are as follows.

1. Set $\beta_0 = 0$ and $\beta_1 = 1$ initially
2. Calculate

$$\bar{\mathbf{r}}(\beta_0) = \boldsymbol{\alpha}_{\mathbf{in}} + \beta_0(\mathbf{r} - \boldsymbol{\alpha}_{\mathbf{in}}); \quad \bar{\mathbf{r}}(\beta_1) = \boldsymbol{\alpha}_{\mathbf{in}} + \beta_1(\mathbf{r} - \boldsymbol{\alpha}_{\mathbf{in}}) \tag{2.52}$$

$$f_m(\beta_0) = \eta(\beta_0) - M_m g(\theta(\beta_0)); \quad f_m(\beta_1) = \eta(\beta_1) - M_m g(\theta(\beta_1)) \tag{2.53}$$

3. Judge whether $\bar{\mathbf{r}}(\beta_0)$ and $\bar{\mathbf{r}}(\beta_1)$ are on either side of the maximum stress ratio surface
   If $f_m(\beta_0)f_m(\beta_1) < 0$ and $f_m(\beta_1) > 0$ go to step 4, else if $f_m(\beta_0)f_m(\beta_1) > 0$ and $f_m(\beta_1) < 0$ then set $\beta_0 = \beta_1$ and $\beta_1 = 2\beta_1$ and go to step 2.
4. Calculate

$$\beta = \beta_1 - \frac{f_b(\beta_1)(\beta_1 - \beta_0)}{f_b(\beta_1) - f_b(\beta_0)} \tag{2.54}$$

$$\bar{\mathbf{r}}(\beta) = \boldsymbol{\alpha}_{\mathbf{in}} + \beta(\mathbf{r} - \boldsymbol{\alpha}_{\mathbf{in}}) \tag{2.55}$$

$$f_m(\beta) = \eta(\beta) - M_m g(\theta(\beta)) \tag{2.56}$$

   If $|f_m(\beta)| < tolerance$, convergence is reached, else go to step 5.
5. Update β_0 and β_1 according to the relative value of $f_m(\beta_0)$, $f_m(\beta_1)$ and $f_m(\beta)$.
   If $f_m(\beta)f_m(\beta_1) < 0$, then $\beta_1 = \beta$ and $f_m(\beta_1) = f_m(\beta)$, then go to step 4; else if $f_m(\beta)f_m(\beta_1) > 0$, then $f_m(\beta_0) = \frac{f_m(\beta_0)f_m(\beta_1)}{f_m(\beta_0) + f_m(\beta_1)}$, $\beta_1 = \beta$ and $f_m(\beta_1) = f_m(\beta)$, go to step 4.

2.4.4 Symmetrisation of the Elastic-Plastic Tangent

As is seen in Eq. (2.51) the tangent operator is not symmetric due to the non-associated flow rule, resulting in an asymmetric system of equations, which is undesirable due to the high computational cost. Various methods that symmetrise non-associated constitutive models have been developed (e.g. Pande and Pietruszczak 1986; Xiong 1986; Luo et al. 2013). In our implementation, the tangent matrix transformation technique developed by Xiong (1986) was adopted, and is expressed as:

$$\mathbf{D}_{\mathbf{ep}} = \mathbf{D}_{\mathbf{e}} - \frac{\mathbf{D}_{\mathbf{e}} : (\mathbf{m} + \frac{D}{3}\mathbf{I}) \otimes (\mathbf{m} + \frac{D}{3}\mathbf{I}) : \mathbf{D}_{\mathbf{e}}}{H + (\mathbf{n} - \frac{1}{3}(\mathbf{r} : \mathbf{n})\mathbf{I}) : \mathbf{D}_{\mathbf{e}} : (\mathbf{m} + \frac{D}{3}\mathbf{I})} \cdot \frac{(\mathbf{n} - \frac{1}{3}(\mathbf{r} : \mathbf{n})\mathbf{I}) : \mathbf{D}_{\mathbf{e}} : \Delta\boldsymbol{\varepsilon}}{(\mathbf{m} + \frac{D}{3}\mathbf{I}) : \mathbf{D}_{\mathbf{e}} : \Delta\boldsymbol{\varepsilon}} \tag{2.57}$$

For the models of piles in liquefiable ground studied in this dissertation, this symmetrisation technique reduces computation time by 35 % on average.

In the OpenSees implementation of the model, an elastic material stage is incorporated into the code to avoid numerical instability in generating the initial stress state, further details of this technique can be found in the OpenSees command manual for the material "CycLiqCPSP" (http://opensees.berkeley.edu).

2.5 Validation of Model Formulation and Implementation

The performance of the model is here evaluated by conducting element experiment simulations and simulation of the VELACS centrifuge shaking table tests.

2.5.1 *Undrained and Drained Triaxial Experiment Simulation*

Triaxial data of undrained and drained loading from Verdugo and Ishihara has been widely used in the evaluation and validation of constitutive models (e.g. Wang et al. 1990; Dafalias and Manzari 2004), as they cover a wide range of confining pressures and initial void ratios. The Toyoura sand used in these experiments had a mean diameter of $D_{50} = 0.17$ mm, maximum and minimum void ratios of 0.977 and 0.597.

The model parameters used in the simulation are provided in Table 2.1. Most parameters for the simulation of Toyoura sand experiments were calculated via previously stated determination methods using experimental data from Zhang (1997) and Zhang et al. (1997) which will be used in the simulations of cyclic torsional tests as well. However, as the Toyoura sand ($D_{50} = 0.18$ mm, $e_{max} = 0.973$ and $e_{min} = 0.635$) used by Zhang et al. varied slightly from that used by Verdugo and Ishihara, and more importantly, the experiments by Zhang et al. and those by Verdugo and Ishihara were conducted using different preparation methods, different dilatancy parameters ($d_{re,1}$, and d_{ir}) were used for the simulation of the two respective sets of experiment (Table 2.1). The critical state parameters (M, λ_c, e_0, ξ) used in the simulations were adopted from the work of Li and Wang (1998) and Li and Dafalias (2000).

Figure 2.5 shows the simulation results of the undrained experiments. With the confining pressure ranging from 0.1 to 3 MPa, and void ratio from 0.907 to 0.735, the model was able to achieve good agreement with experiment data using a single set of model parameters. Thus proving the proposed model to be capable in the simulation of highly dilative and contractive sand behaviour. The unloading processes were also simulated, exhibiting the effectiveness of the reversible and irreversible dilatancy formulations in the model.

Table 2.1 Model parameters for the simulations of element and centrifuge experiments

Sand	G_o	κ	h	M	$d_{re,1}$	$d_{re,2}$	d_{ir}	α	$\gamma_{d,r}$	n^p	n^d	λ_c	e_0	ξ
Toyoura[a]	200	0.008	1.8	1.25	0.6	30	1.4	20	0.05	1.1	7.8	0.019	0.934	0.7
Toyoura[b]	200	0.008	1.8	1.35	0.35	30	0.75	20	0.05	1.1	7.8	0.019	0.934	0.7
Nevada	225	0.004	1.7	1.35	0.8	30	0.6	10	0.05	1.1	8.0	0.029	0.843	0.7

[a]Toyoura sand used by Verdugo and Ishihara (1996)

[b]Toyoura sand used by Zhang et al. (1997) and Chiaro et al. (2013)

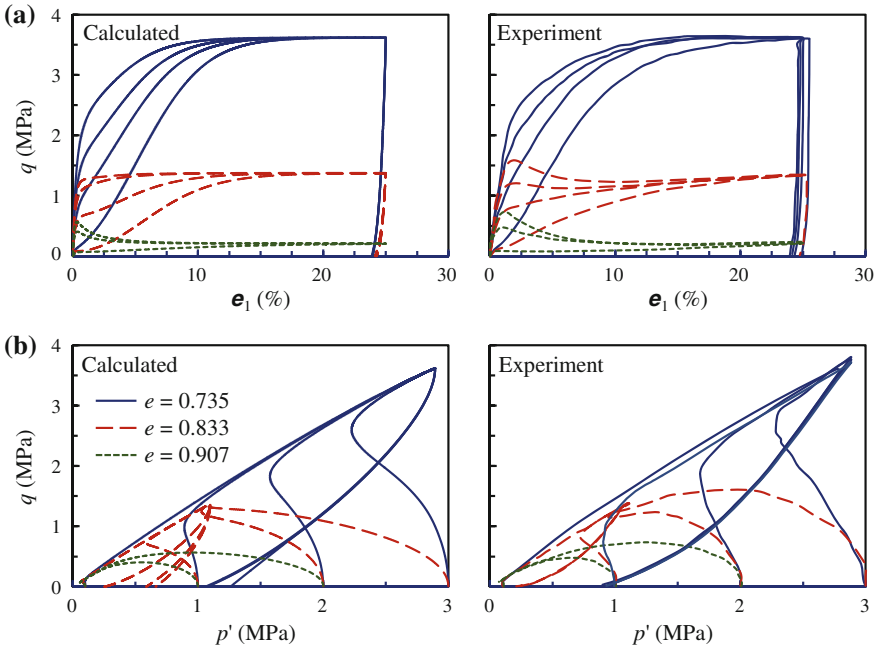

Fig. 2.5 Simulation of undrained triaxial tests on Toyoura sand of different void ratio and initial effective confining pressure (experiment data from Verdugo and Ishihara 1996)

Drained triaxial experiment simulations are presented in Fig. 2.6. Again, the proposed model showed good agreement with experiment data over a range of initial void ratios and confining pressures during both the loading and unloading stages. These simulation results are comparable to those of existing models well known for their simulative capabilities under such stress paths (e.g. Dafalias and Manzari 2004).

2.5.2 *Undrained Cyclic Torsional Experiment Simulation*

Two undrained hollow cylinder cyclic torsional experiments were simulated using the proposed model to evaluate its capabilities in modelling the cyclic response, and especially the large post-liquefaction shear deformation of sand. The experiments were on Toyoura sand of different densities by Zhang et al. (1997).

The two tests on Toyoura sand were conducted on sand of 60 and 48 % respectively, with the shear stress amplitude for the tests being 25 kPa, and the initial consolidation stress were 100 kPa. The model parameters used are provided in Table 2.1, which were determined as mentioned previously. Figures 2.7 and 2.8 compares the calculated stress path and stress-strain relationship with experiment

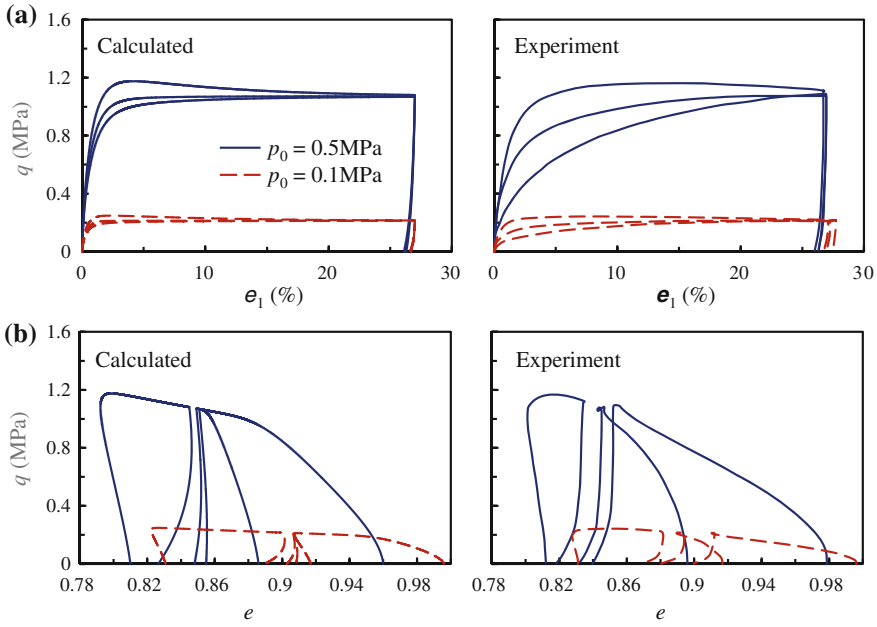

Fig. 2.6 Simulation of drained triaxial tests on Toyoura sand of different void ratio and initial effective confining pressure (experiment data from Verdugo and Ishihara 1996)

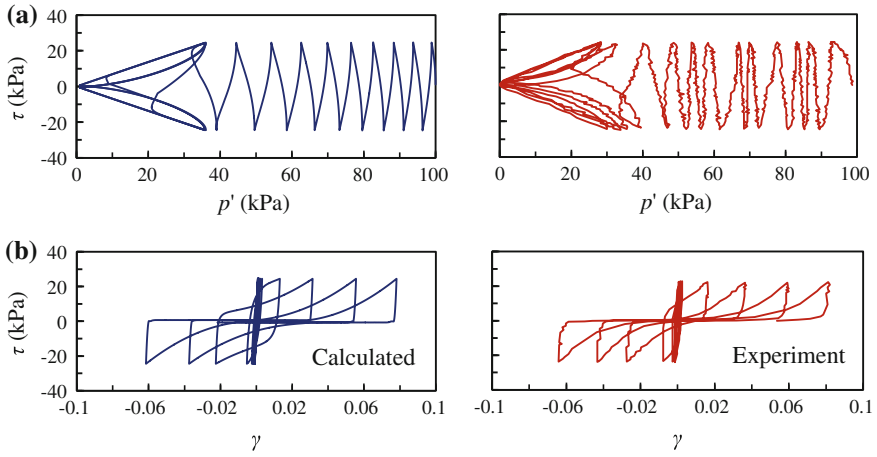

Fig. 2.7 Simulation of undrained cyclic torsional test for Toyoura sand at Dr = 60 % (experiment data from Zhang et al. 1997)

results of Toyoura sand at 60 and 48 % relative density, and shows excellent agreement between them. The model fully captures the features of cyclic mobility of sand during loading and reverse loading. It is worth noting that the generation of shear

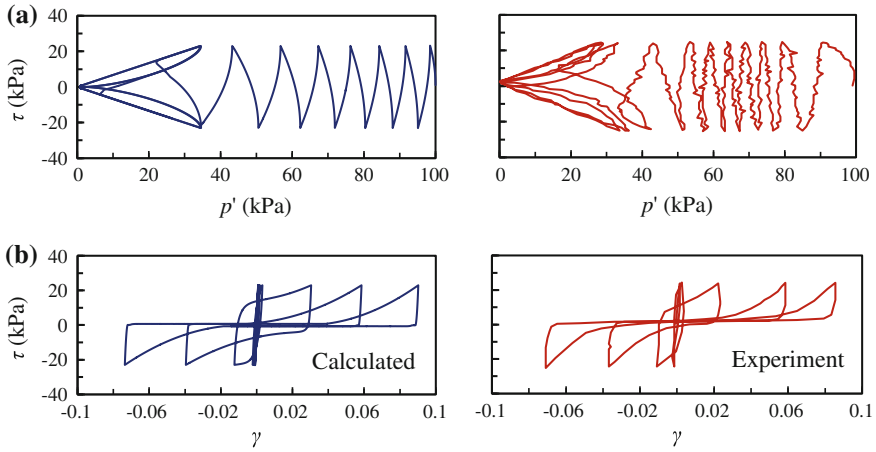

Fig. 2.8 Simulation of undrained cyclic torsional test for Toyoura sand at Dr = 48 % (experiment data from Zhang et al. 1997)

strain at zero effective stress after initial liquefaction and its accumulation with the increasing number of load cycles is very well simulated. This feature is a great advantage of this model over most existing models which either are unable to simulate the accumulation of shear strain at zero effective stress (e.g. Papadimitriou et al. 2001; Dafalias and Manzari 2004) or artificially generate the shear strain at non-liquefaction state (e.g. Elgamal et al. 2002; Boulanger and Ziotopoulou 2013). Again, for the simulation of cyclic tests on Toyoura sand of different densities, the same set of parameters were used due to appropriate incorporation of critical state behaviour.

To display the ability of the model in modelling large shear strains, an undrained cyclic torsional test with a static shear stress bias for Toyoura sand at D_r = 46.6 % conducted by Chiaro et al. (2013) was simulated. The preparation method for the sample used in the test was through air pluviation, which was the same as that of Zhang's experiments, hence the same parameters were used. Figure 2.9 shows the shear strain accumulation reached 32 % in both the experiment and simulation. However, for more accurate reflection of such or even higher levels of shear strain, geometric nonlinearity should be taken into consideration for both the constitutive model and the finite element formulation, which is beyond the scope of the current study.

2.5.3 VELACS Centrifuge Experiment Simulation

To validate the performance of the proposed model and numerical algorithm in boundary value problems, the well documented VELACS centrifuge Model No.1 and Model No.2 were simulated and compared against RPI's experiment data (Taboada and Dobry 1993a, b). The basic setup of the centrifuge models are shown

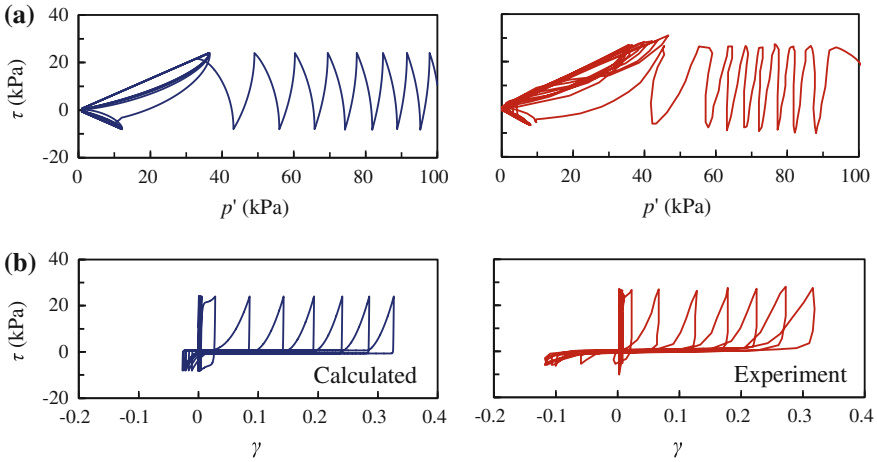

Fig. 2.9 Simulation of undrained cyclic torsional test with a static shear stress bias for Toyoura sand at Dr = 46.6 % (experiment data from Chiaro et al. 2013)

in Fig. 2.10, the two models were almost identical apart from the fact that Model No. 2 had a slight inclination of 2°.

Since the centrifuge experiments were conducted in laminar boxes, they represent the one-dimensional seismic response of a liquefiable soil layer, and thus can be simulated using one single column of elements with properly set boundary conditions. In the simulations presented, three-dimensional Brick UP elements (Yang et al. 2008) with side length of 1.0 m were used to evaluate the performance of the model in 3D analysis. Figure 2.11 shows the finite element mesh, with its boundary conditions. The 4 nodes at the base of the finite element mesh were fixed to follow the input motion, the nodes on each level is then tied together using the Equal DOF command in OpenSees (McKenna and Fenves 2001). Free drainage was set at the top of the model, the rest of the boundary were undrained. For Model No. 2, the direction of gravity was tilted 2° as shown in Fig. 2.11. In the simulations, a gravity loading step was carried out with an elastic material stage and then with a plastic material stage as aforementioned to create the initial geostatic stress field. Ground motion for the two experiments were input at the base of the mesh using the actual input accelerations reported by Taboada and Dobry (1993a, b).

Nevada sand of 45 % relative density ($e = 0.724$) was used in both experiments. The model parameters were estimated based on experiment results (Arulmoli et al. 1992; Kutter et al. 1994), and are shown in Table 2.1. For permeability, an important parameter in the simulation, there has been various values reported for Nevada sand at such relative density, ranging from 1.05×10^{-3} m/s to 3.3×10^{-3} m/s (Bardet et al. 1993; Kutter et al. 1994; Taboada and Dobry 1998; etc.), Manzari and Arulanandan (1993), Andrianopoulos et al. (2010) suggested using time dependent permeability during liquefaction. For simplicity, the permeability k was set to be 1.6×10^{-3} m/s in between the various reported values.

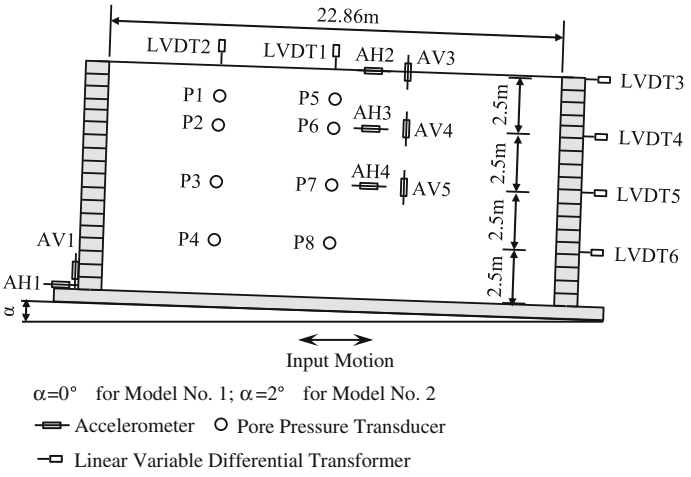

Fig. 2.10 Test configurations of VELACS centrifuge Model No. 1 and Model No. 2

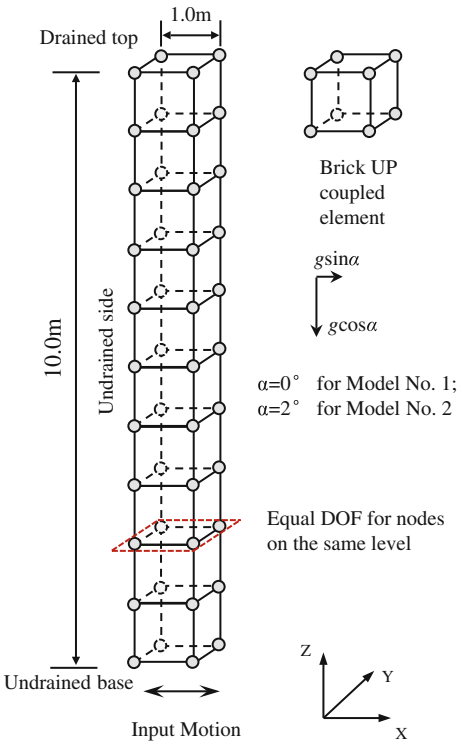

Fig. 2.11 Finite element mesh using coupled 3D Brick UP element for Model No. 1, Model No. 2 and a three dimensional site response analysis

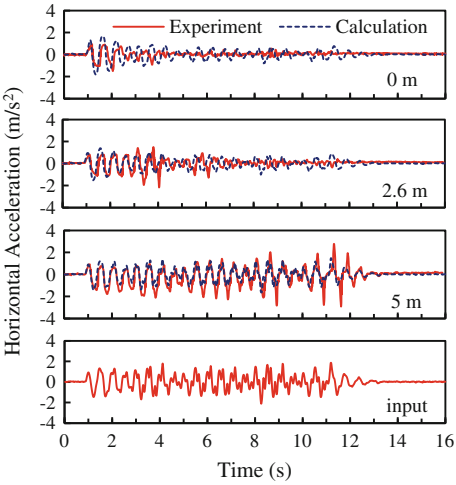

Fig. 2.12 Calculated and measured horizontal acceleration histories in Model No. 1

For the simulation of centrifuge Model No. 1, the calculated ground acceleration at three different depth are compared with recorded data in Fig. 2.12, showing satisfactory agreement. The attenuation of acceleration was notable in both the experiment data and simulation. The amplitude of the simulated lateral displacements were somewhat smaller than the experiment recordings, though final residual lateral displacements matched well (Fig. 2.13). Figure 2.14 shows the excess pore pressure time histories, excellent agreement between experiment and simulation results can be observed for the generation and dissipation process of excess pore pressure. It can been seen that soils above 5 m in depth all reached liquefaction

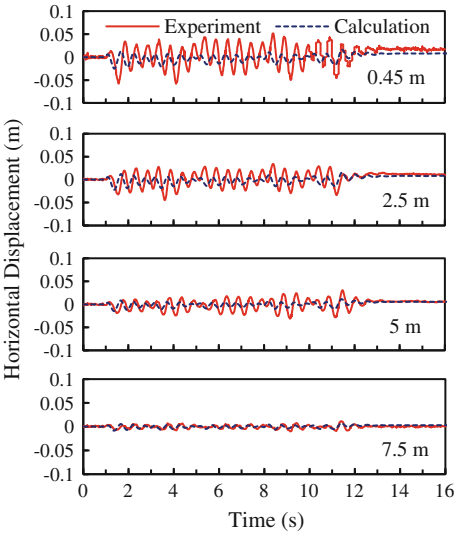

Fig. 2.13 Calculated and measured horizontal displacement histories in Model No. 1

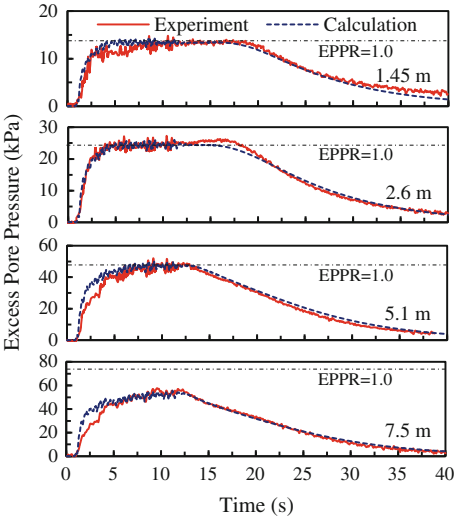

Fig. 2.14 Calculated and measured excess pore pressure histories in Model No. 1

during the seismic event, and the time needed to reach liquefaction was less with smaller depth. Figure 2.15 shows typical stress path and stress-strain relations at two different depths in Model No. 1, showing typical patterns of stiffness degradation during pore pressure build up. From Fig. 2.15, it can be clearly seen that soil reached liquefaction at 2.5 m depth and did not reach liquefaction at 7.5 m.

Figure 2.16 shows that the simulated soil settlement in Model No. 1 is significantly different to that measured in the experiment. In the experiment, settlement developed very quickly, reaching 22 cm after only 20 s, however, the calculated final settlement was only half of that, and reached its final value after 40 s. This discrepancy between simulated settlement and measured settlement in centrifuge tests has been observed in the application of many plasticity models for sand, and

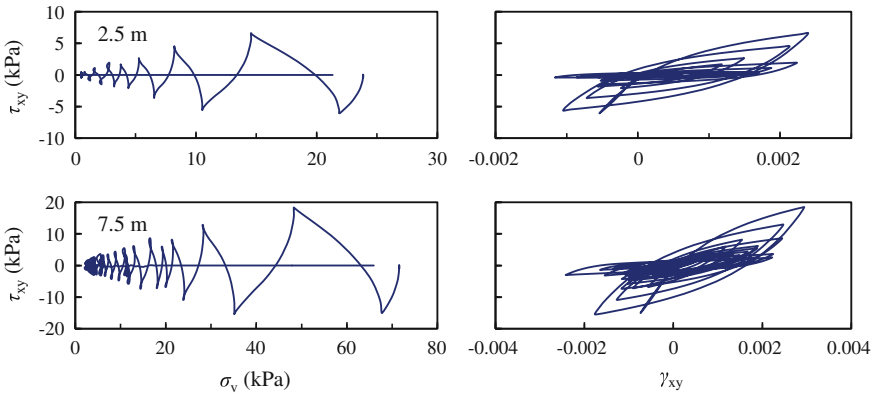

Fig. 2.15 Typical stress path and stress-strain relations at various depths in Model No. 1

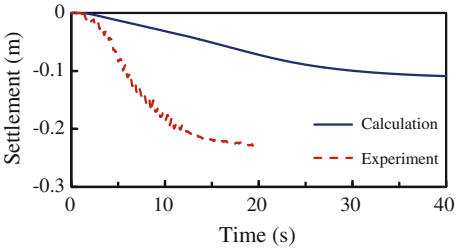

Fig. 2.16 Calculated and measured soil settlement in Mode No. 1

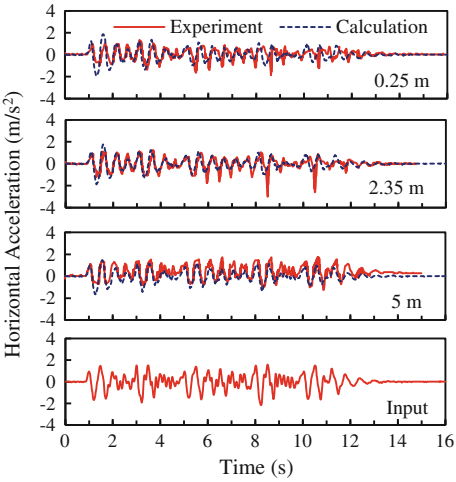

Fig. 2.17 Calculated and measured acceleration histories in Model No. 2

has been an issue of debate: (1) Zhang and Wang (2012) indicated that this difference may be caused by rate effects due to the high velocities in the centrifuge tests; (2) Boulanger and Ziotopoulou (2013) pointed out that the sedimentation process is not reflected in constitutive models; (3) Elgamal et al. (2003) assumes that the underestimation of settlement is due to the high nonlinearity of actual sand; (4) Shahir et al. (2012) tended to suggest that the change in the permeability of sand during liquefaction plays and important role.

In the simulation of Model No. 2, Fig. 2.17 again shows the good agreement for acceleration between experiment and calculation results. The trend and final residual value of the lateral displacements were well simulated (Fig. 2.18). The excess pore pressure time histories are shown in Fig. 2.19, with the patterns of excess pore pressure very closely simulated. The typical stress path and stress-strain relations shown in Fig. 2.20 were different from those of Model No. 1, as the ground inclination caused shear strain to accumulate in one direction, leading to the large lateral deformation in Fig. 2.21. Again, the simulation underestimates the settlement of the sand (Fig. 2.22).

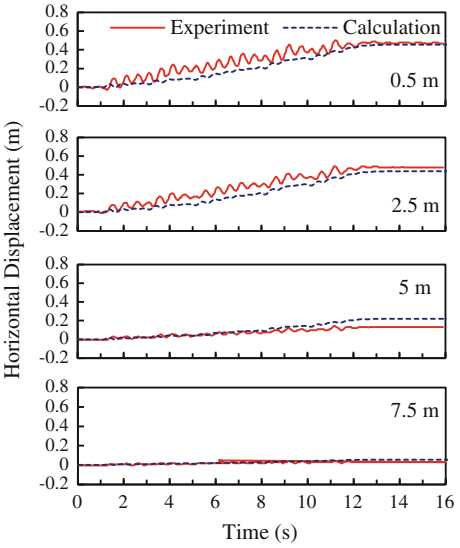

Fig. 2.18 Calculated and measured horizontal displacement histories in Model No. 2

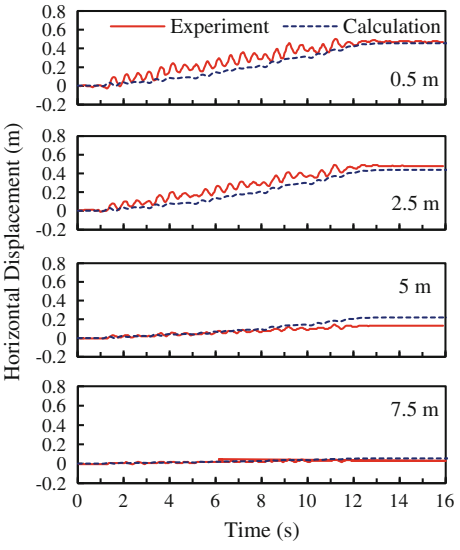

Fig. 2.19 Calculated and measured excess pore pressure histories in Model No. 2

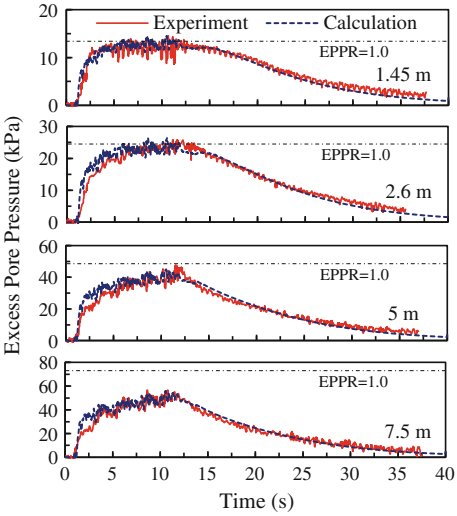

Fig. 2.20 Calculated and measured excess pore pressure histories in Model No. 2

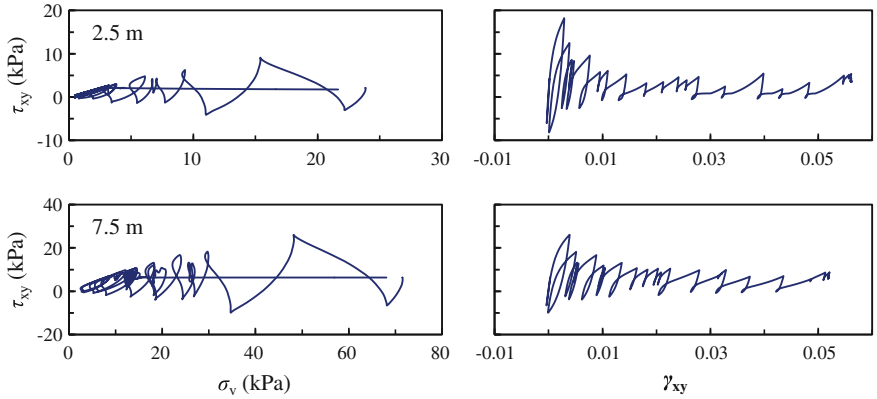

Fig. 2.21 Typical stress path and stress-strain relations in Model No. 2

Fig. 2.22 Calculated and measured soil settlement in Mode No. 2

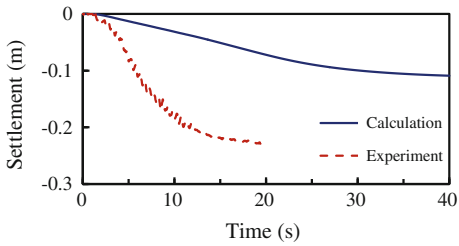

2.6 Summary

This chapter presents the formulation and numerical implementation of a unified constitutive model for seismic liquefaction analysis based on the physics of post-liquefaction deformation established by Zhang and Wang (2012). The model is unique in that it provides a unified description of sand of different conditions from pre- to post-liquefaction under monotonic and cyclic loading.

By enforcing the volumetric compatibility equation at liquefaction according to Zhang and Wang's (2012) proposition, the model provides physically based computation of the generation and accumulation of shear strain at zero effective stress, which is a significant advantage over most existing models.

Through the appropriate formulation of two dilatancy components, namely reversible and irreversible, the model explicitly links the phenomenon of cyclic mobility to soil dilatancy, providing excellent modelling capabilities for both monotonic and cyclic response of sand.

The state parameter Ψ was incorporated into the model for compatibility with the critical state soil mechanics concept. The model was unified to allow the simulation of sand at different relative densities and confining pressures with a same set of parameters.

In the multiaxial formulation, the mapping rules for plasticity and dilatancy were proposed to be suitable in three dimensional space and accommodate the three dimensional numerical implementation of the model. Calibration methods for the model parameters were also provided.

Using a cutting-plane algorithm with substepping as the stress integration scheme, and the Pegasus procedure to locate the projection of current stress state on the maximum stress ratio surface, the model was implemented in the OpenSees finite element framework, making it openly available to the technical community.

The constitutive model and its three dimensional numerical implementation were validated against drained and undrained triaxial experiments, undrained cyclic torsional experiments and centrifuge experiments, showing the great capabilities of the model in simulating sand response of a wide range of densities and confining pressure, and highlighting its advantage in simulating large post-liquefaction shear deformations.

However, as the current model underestimates the reconsolidation settlement of sand, which is something that could be looked into in future improvements.

References

Andrianopoulos KI, Papadimitriou AG, Bouckovalas GD. Explicit integration of bounding surface model for the analysis of earthquake soil liquefaction. Int J Numer Anal Meth Geomech. 2010;34(15):1586–614.

Arulmoli K, Muraleetharan KK, Hossain MM, Fruth LS. VELACS: verification of liquefaction analysis by centrifuge studies, Laboratory testing program, Soil Data Report, The Earth Technology Corporation, Project No. 90-0562, Irvine, California; 1992.

Bardet JP, Huang Q, Chi SW. Numerical predictions for Model No. 1. In: Proceedings, international conference on verification of numerical procedures for the analysis of soil liquefaction problems, vol. 1; 1993. pp. 67–86.
Been K, Jefferies MG. A state parameter for sands. Geotechnique. 1985;35(2):99–112.
Boulanger RW, Ziotopoulou K. Formulation of a sand plasticity plane-strain model for earthquake engineering applications. Soil Dyn Earthq Eng. 2013;53:254–67.
Chiaro G, Kiyota T, Koseki J. Strain localization characteristics of loose saturated Toyoura sand in undrained cyclic torsional shear tests with initial static shear. Soils Found. 2013;53(1):23–34.
Dafalias YF, Manzari MT. Simple plasticity sand model accounting for fabric change effects. J Eng Mech. 2004;130(6):622–34.
Dafalias YF, Popov EP. A model of nonlinearly hardening materials for complex loading. Acta Mech. 1975;21(3):173–92.
Dowell M, Jarratt P. The, "Pegasus" method for computing the root of an equation. Bit Numer Math. 1972;12(4):503–8.
Elgamal A, Yang Z, Parra E. Computational modeling of cyclic mobility and post-liquefaction site response. Soil Dyn Earthq Eng. 2002;22(4):259–71.
Elgamal A, Yang Z, Parra E, Ragheb A. Modeling of cyclic mobility in saturated cohesionless soils. Int J Plast. 2003;19(6):883–905.
Kutter BL, Chen Y, Shen CK. Triaxial and torsional shear test results for sand. Naval Facilities Engineering Service Center, Contact Report CR 94.003-SHR, Port Hueneme, California; 1994.
Li XS, Dafalias YF. Dilatancy for cohesionless soils. Geotechnique. 2000;50(4):449–60.
Li XS, Wang Y. Linear representation of steady-state line for sand. J Geotech Geoenviron Eng. 1998;124(12):1215–7.
Ling HI, Yang S. Unified sand model based on the critical state and generalized plasticity. J Eng Mech. 2006;132:1380–91.
Luo T, Qin Z, Feng X, Xia F, Yao Y, Sheng D. A symmetrisation method for non-associated unified hardening model. Comput Geotech. 2013;52:38–45.
Manzari MT, Arulanandan K. Numerical predictions for Model No. 1. In: Proceedings, international conference on verification of numerical procedures for the analysis of soil liquefaction problems, vol. 1; 1993. pp. 179–185.
McGann CR, Arduino P, Mackenzie-Helnwein P. Stabilized single-point 4-node quadrilateral element for dynamic analysis of fluid saturated porous media. Acta Geotech. 2012:1–15.
McKenna F, Fenves GL. OpenSees Manual. PEER Center. 2001. http://OpenSees.berkeley.edu.
Pande GN, Pietruszczak ST. Symmetric tangential stiffness formulation for non-associated plasticity. Comput Geotech. 1986;2(2):89–99.
Papadimitriou AG, Bouckovalas GD, Dafalias YF. Plasticity model for sand under small and large cyclic strains. J Geotech Geoenviron Eng. 2001;127(11):973–83.
Richart FE Jr, Hall JR, Woods RD. Vibrations of soils and foundations. New Jersey: Prentice-Hall Inc; 1970.
Roscoe KH, Schofield AN, Wroth CP. On the yielding of soils. Geotechnique. 1958;8(1):22–53.
Rowe PW. The stress-dilatancy relation for static equilibrium of an assembly of particles in contact. In: Proceedings of the Royal Society of London. Series a. Mathematical and physical sciences, London, vol. 269(1339); 1962. pp. 500–527.
Schofield AN, Wroth CP. Critical state soil mechanics. London: McGraw-Hill; 1968.
Shahir H, Pak A, Taiebat M, Jeremic B. Evaluation of variation of permeability in liquefiable soil under earthquake loading. Comput Geotech. 2012;40:74–88.
Shamoto Y, Zhang JM. Mechanism of large post-liquefaction deformation in saturated sands. Soils Found. 1997;2(37):71–80.
Simo JC, Ortiz M. A unified approach to finite deformation elastoplastic analysis based on the use of hyperelastic constitutive equations. Comput Meth Appl Mech Eng. 1985;49(2):221–45.
Sloan SW, Abbo AJ, Sheng D. Refined explicit integration of elastoplastic models with automatic error control. Eng Comput. 2001;18(1/2):121–54.

Taboada VM, Dobry R. Experimental results of Model No. 1 at RPI. In: Proceedings, international conference on verification of numerical procedures for the analysis of soil liquefaction problems, vol. 1; 1993a. pp. 3–17.

Taboada VM, Dobry R. Experimental results of Model No. 2 at RPI. In: Proceedings, international conference on verification of numerical procedures for the analysis of soil liquefaction problems, vol. 1; 1993b. pp. 277–294.

Taboada VM, Dobry R. Centrifuge modeling of earthquake-induced lateral spreading in sand. J Geotech Geoenviron Eng. 1998;124(12):1195–206.

Verdugo R, Ishihara K. The steady state of sandy soils. Soils Found. 1996;36(2):81–92.

Wang ZL, Dafalias YF, Shen CK. Bounding surface hypoplasticity model for sand. J Eng Mech. 1990;116(5):983–1001.

Xiong WL. Symmetric formulation of tangential stiffnesses for non-associated plasticity. Appl Math Mech. 1986;7(11):1043–52.

Yang Z, Lu J, Elgamal A. OpenSees soil models and solid-fluid fully coupled elements user manual. University of California, San Diego, California. 2008. http://cyclic.ucsd.edu/opensees/OSManual_UCSD_soil_models_2008.pdf.

Zhang JM. Cyclic critical stress state theory of sand with its application to geotechnical problems. Ph. D thesis, Tokyo Institute of Technology, Tokyo; 1997.

Zhang JM, Wang G. Large post-liquefaction deformation of sand, part I: physical mechanism, constitutive description and numerical algorithm. Acta Geotech. 2012;7(2):69–113.

Zhang JM, Shamoto Y, Tokimatsu K. Moving critical and phase-transformation stress state lines of saturated sand during undrained cyclic shear. Soils Found. 1997;2(37):51–9.

http://www.springer.com/978-3-662-49661-9

Single Piles in Liquefiable Ground
Seismic Response and Numerical Analysis Methods
Wang, R.
2016, XVII, 119 p. 101 illus., 75 illus. in color.,
Hardcover
ISBN: 978-3-662-49661-9